Delft University of Technology

Study on Characteristics and UIS of Hexagonal Planar SiC VDMOSFETs With Varied JFET Width

Luo, Hou-Cai; Wu, Huan; Zhang, Jing-Ping; Zheng, Bo-Feng; Lang, Lei; Zhang, Guo-Qi; Chen, Xian-Ping

DOI
10.1109/TDMR.2024.3388482

Publication date
2024

Document Version
Final published version

Published in
IEEE Transactions on Device and Materials Reliability

Citation (APA)
Luo, H.-C., Wu, H., Zhang, J.-P., Zheng, B.-F., Lang, L., Zhang, G.-Q., & Chen, X.-P. (2024). Study on Characteristics and UIS of Hexagonal Planar SiC VDMOSFETs With Varied JFET Width. *IEEE Transactions on Device and Materials Reliability*, *24*(2), 323-328. https://doi.org/10.1109/TDMR.2024.3388482

Important note
To cite this publication, please use the final published version (if applicable).
Please check the document version above.

Copyright
Other than for strictly personal use, it is not permitted to download, forward or distribute the text or part of it, without the consent of the author(s) and/or copyright holder(s), unless the work is under an open content license such as Creative Commons.

Takedown policy
Please contact us and provide details if you believe this document breaches copyrights.
We will remove access to the work immediately and investigate your claim.

This work is downloaded from Delft University of Technology.
For technical reasons the number of authors shown on this cover page is limited to a maximum of 10.

Green Open Access added to TU Delft Institutional Repository

'You share, we take care!' - Taverne project

https://www.openaccess.nl/en/you-share-we-take-care

Otherwise as indicated in the copyright section: the publisher
is the copyright holder of this work and the author uses the
Dutch legislation to make this work public.

Study on Characteristics and UIS of Hexagonal Planar SiC VDMOSFETs With Varied JFET Width

Hou-Cai Luo, Huan Wu, Jing-Ping Zhang, Bo-Feng Zheng, Lei Lang, Guo-Qi Zhang, *Fellow, IEEE*, and Xian-Ping Chen, *Member, IEEE*

***Abstract*—The hexagonal cell topology of planar SiC VDMOSFETs with varied JFET width (L_{JFET}) are designed and manufactured in this study. $L_{JFET} = 1.4\mu m$ has the best HF-FOM ($R_{on}\times C_{gd}$) and HF-FOM ($R_{on}\times Q_{gd}$) by comparing the dynamic and static parameters of each design. Besides, the UIS reliability and failure mechanism for series designs are investigated by experiment and TCAD simulation. The results show that the high temperature is generated by energy dissipation during avalanche and it drives the parasitic BJT conduction, causing I_{ds} out of control and instantaneous heat concentration in a very short time. The extremely high temperature causes internal cracking of the material and metal melting, resulting in gate-source short circuit and device damage. It would provide suggestions for device design and reliability consideration.**

***Index Terms*—SiC VDMOSFET, hexagonal cell topology, avalanche reliability, BJT, UIS.**

I. Introduction

SILICON carbide metal-oxide-semiconductor field-effect transistors (SiC MOSFETs) present one of excellent potential candidates to replace silicon-based insulated gate bipolar transistors (Si IGBTs) in power electronics due to their fast switching frequency, low dissipating power, high thermal conductivity, and large current density [1]. These outstanding features of SiC MOSFETs are due to the properties of SiC material. There are wider band gap, higher thermal conductivity, larger critical electric field strength in SiC material compared with that of Si. Due to these exceptional properties, SiC MOSFETs have significant potential in power systems, such as electric vehicles, charging stations, and photovoltaic inverters [2]. Over the years, advancements in design and fabrication technology have led to the commercialization of SiC MOSFETs in the power electronics market.

Two main technology directions exist in SiC MOSFETs, distinguished by differences in their gate electrode structure: planar gate structure (simplified SiC VDMOSFET) and trench gate structure (simplified SiC UMOSFET) [3]. In comparison to SiC VDMOSFETs, SiC UMOSFETs exhibit higher power density and lower ON-resistance. However, the SiC UMOSFETs are less robust in the blocking state as the gate oxide has to withstand a higher electric field. The gate oxide electric field in planar SiC VDMOSFETs is substantially decreased by reducing the distance between the two P-Based regions, also known as JFET width, abbreviated as L_{JFET} in this study. The conductivity of SiC VDMOSFETs is decrease as the narrow L_{JFET}. However, the electric field strength maintained by the gate oxide during the avalanche breakdown condition would increase as the L_{JFET} increases. If the L_{JFET} is too large, the device may easily suffer damage from gate oxide breakdown [4]. The L_{JFET} geometric parameter is critical in balancing the conduction characteristics and reliability of SiC VDMOSFETs [5]. Moreover, the characteristics of SiC VDMOSFETs are not only impacted by L_{JFET}, but also by different cell topologies. Compared to the linear strip distribution, the hexagonal topology distribution provides a higher cell density and improves conduction characteristics in SiC VDMOSFETs according to previous studies [6], [7]. In the case of 1.2kV SiC VDMOSFETs with $L_{JFET} = 1.4\mu m$, the hexagonal topology demonstrates 58.7% lower specific ON resistance compared to the linear topology [8]. Therefore, the hexagonal topology is a crucial aspect to be taken into consideration while designing SiC VDMOSFETs.

Reliability is a critical issue in the power system, especially for SiC MOSFETs. Numerous studies have investigated reliability and failure mechanisms, including short circuit [9], surge current [10], avalanche [11], gate oxide stress [12], [13], and so on. Additionally, previous studies [14], [15] have explored how L_{JFET} impact device performance and reliability, with a focus on short-circuits and avalanche. However, it is worth noting that all prior research on avalanche reliability has solely

Manuscript received 31 January 2024; accepted 8 April 2024. Date of publication 16 April 2024; date of current version 20 June 2024. This work was supported in part by the General Fund for Pre-Research of Military Program under Grant 61404140404; in part by the General Program of National Natural Science Foundation of China under Grant 62071073; in part by the Frontier Innovation Program (National Defense Science and Technology Innovation Special Zone) under Grant 19-163-00-KX-002-024-01; in part by the Key Laboratory Open Fund under Grant GD20201; and in part by the Chongqing Municipal Technology Innovation and Application Development Program (Military-Civilian Integration) under Grant JG2021083. *(Hou-Cai Luo and Huan Wu contributed equally to this work.) (Corresponding author: Xian-Ping Chen.)*

Hou-Cai Luo, Huan Wu, Jing-Ping Zhang, Lei Lang, and Xian-Ping Chen are with the Key Laboratory of Optoelectronic Technology and Systems, Education Ministry of China, and the College of Optoelectronic Engineering, Chongqing University, Chongqing 400044, China (e-mail: xianpingchen@cqu.edu.cn).

Bo-Feng Zheng is with the LAB 2020, Chongqing Pingchuang Institute of Semiconductors Company Ltd., Chongqing 402760, China.

Guo-Qi Zhang is with the Delft Institute of Microsystems and Nanoelectronics, Delft University of Technology, 2628 CD Delft, The Netherlands.

Color versions of one or more figures in this article are available at https://doi.org/10.1109/TDMR.2024.3388482.

Digital Object Identifier 10.1109/TDMR.2024.3388482

1530-4388 © 2024 IEEE. Personal use is permitted, but republication/redistribution requires IEEE permission.
See https://www.ieee.org/publications/rights/index.html for more information.

Authorized licensed use limited to: TU Delft Library. Downloaded on July 10,2024 at 16:24:41 UTC from IEEE Xplore. Restrictions apply.

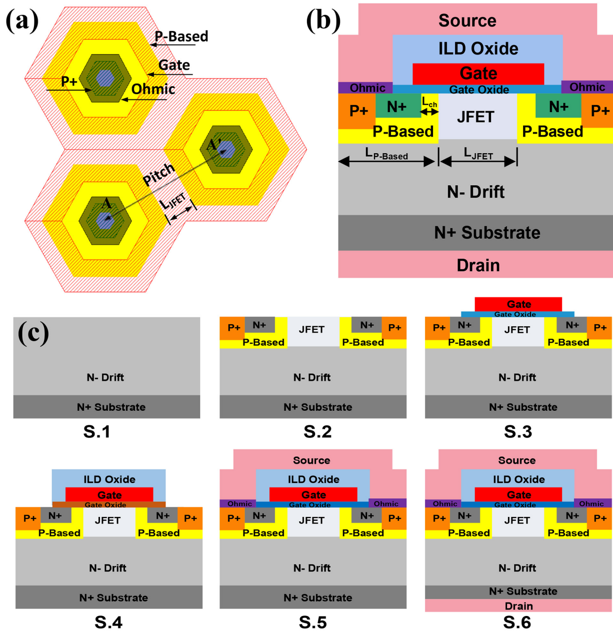

Fig. 1. (a) The hexagonal cell topology, (b) cross section of A-A', (c) the key stages for manufacturing process of SiC VDMOSFETs.

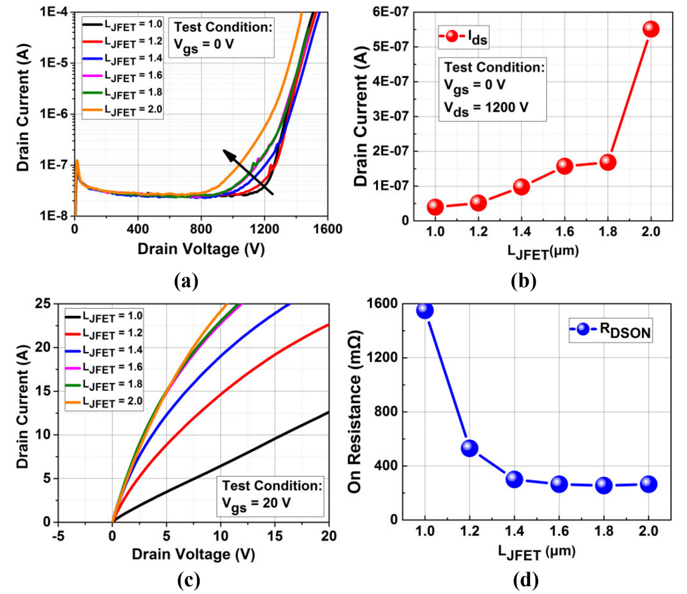

Fig. 2. (a) Blocking characteristic of DUTs and (b) I_{ds} at V_{ds}= 1200V, V_{gs} = 0V as a function of L_{JFET}. (c) Output characteristic of DUTs at V_{gs} = 20V, I_{ds} = 5A. (d) Specific ON resistance of DUTs as a function of L_{JFET}.

concentrated on the conventional linear topology [15]. The characteristics and avalanche reliability of SiC VDMOSFETs with hexagonal topology is seldom. Therefore, this study analyzes the static properties and dynamic characteristics of SiC VDMOSFETs with hexagonal topology and different L_{JFET}. In addition, avalanche capability and failure mechanisms are also investigated by using unclamped inductive switching (UIS) test and technology computer-aided design (TCAD) simulation.

II. Device Structure and Fabrication

The hexagonal cell topology in 1200V SiC VDMOSFETs with various L_{JFET} (1.0μm, 1.2μm, 1.4μm, 1.6μm, 1.8μm, 2.0μm) are designed and fabricated. The topology is illustrated in Fig. 1(a) and (b) alongside the cross section of SiC VDMOSFETs, showcasing the P-Based, Gate, Ohmic, and P+ regions. The distance from A to A' marks the cell pitch. The channel region width is L_{ch}, which equals 0.5μm. The P-Based region width is $L_{P\text{-}Based}$, which is equal to 3.3μm.

Based on the previous design, SiC VDMOSFET chips with a hexagonal cell topology and a blocking voltage of 1200V are manufactured. The key stages of fabrication are shown in Fig. 1(c), including 6 steps. S.1: An epitaxial layer thickness of 10μm with a concentration of 8e15 cm^{-3} is grown on a 6-inch SiC wafer. The wafer is cleaned, followed by etching of aligned marks. S.2: Ion implantation is performed in the P+ source region and P-Based region using a self-aligned process that creates 0.5μm spacers via polysilicon deposition and etching. Then, N+ source ion implantation is employed to form a conduct channel in P-based region. Additionally, slight N-type implantation is executed in the JFET region to enhance the dopant concentration and adjust the threshold voltage. S.3: Gate oxide is formed through thermal oxidation, and the wafer is annealed in a NO atmosphere in order to reduce SiC/SiO_2 defects. Polysilicon is then deposited and etched to produce the gate electrode. S.4: An isolated oxide layer (ILD) is subsequently formed on the polysilicon to protect the gate structure, and then it is etched between the gate and source. S.5: The source ohmic contact is established via rapid thermal annealing. To create source and gate pads, a 4μm-thick AlSiCu layer is deposited. Nitride and polymide deposition are utilized to protect the chip termination, and front-side processing is finished. S.6: The SiC wafer is then thinned to decrease conduction resistance from 350μm to 180μm. Laser annealing is used to activate the ohmic contact, and backside metallization for the drain electrode is deposited, signaling the end of the fabrication process. After production, they are packed into a TO247-3.

III. Device Characterization

This study tested fabricated devices with different L_{JFET} characteristics, measuring various parameters such as drain voltage versus drain current (I_{ds}-V_{ds}), leakage current versus JFET width characteristic (I_{ds}-L_{JFET}), output characteristics (I_{ds}-V_{ds}@V_{gs}), and specific ON-resistance versus JFET width ($R_{on,sp}$-L_{JFET}). The obtained results are depicted in Fig. 2. The drain-source leakage current remains almost constant below 800V, but gradually increased with L_{JFET} increment when V_{ds} was greater than 800V. All designs exhibit blocking voltages above 1200V for $I_{ds} \geq 10\mu$A, with Fig. 2 (b) displaying the extracted leakage current at V_{ds} = 1200V. Additionally, Fig. 2(c) shows the output characteristics under conditions of V_{gs} = 20V measurement. The $R_{on,sp}$ characteristics of L_{JFET} are shown in Fig. 2(d), based on the results obtained at V_{gs} = 20V and I_{ds} = 5A. As the size of L_{JFET} increases from 1.0μm to 1.4μm, there is a marked decrease in $R_{on,sp}$. Conversely,

Authorized licensed use limited to: TU Delft Library. Downloaded on July 10,2024 at 16:24:41 UTC from IEEE Xplore. Restrictions apply.

TABLE I
SUMMARY OF EXPERIMENTAL RESULTS

	L_J1.4	H_J1.0	H_J1.2	H_J1.4	H_J1.6	H_J1.8	H_J2.0
JFET density	0.079	0.144	0.166	0.187	0.207	0.226	0.242
BV [V]	1546	1510	1523	1550	1510	1506	1435
Vth [V]	3.21	3.21	3.2	3.24	3.26	3.24	3.24
$R_{on,sp}$ [mΩ-cm^2]	20.8	44.8	15.3	8.7	7.7	7.4	7.7
$C_{gd,sp}$ [pF/cm^2]	173	164	175	210	247	260	271
$Q_{gd,sp}$ [nC/cm^2]	368	283	377	424	490	520	541
FOM ($R_{on}\times C_{gd}$) [mΩ-pF]	3590	7332	2674	1830	1902	1926	2086
FOM ($R_{on}\times Q_{gd}$) [mΩ-nC]	7662	12680	5760	3685	3770	3849	4164

*Note: L_J1.4 represents linear strip cell topology with L_{JFET} = 1.4µm. H_J1.0 represents hexagonal cell topology with L_{JFET} = 1.0µm. BV@I_{ds} = 100µA. $C_{gd,sp}$@ V_{ds} = 800V.

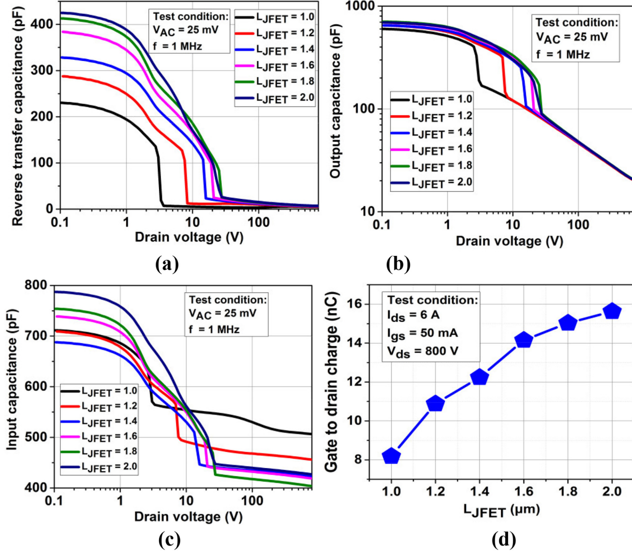

Fig. 3. (a) Reverse transfer capacitance, (b) output capacitance, and (c) input capacitance characteristics of DUTs. (d) Gate to drain charge characteristics versus L_{JFET}.

there is a gradual decrease from 1.6μm to 2.0μm, indicating that the resistance of the JFET region has a relatively insignificant effect. The threshold voltage (V_{th}) is a crucial parameter, extracted under the condition of $V_{gs} = V_{ds}$ @ $I_{ds} = 2$mA. The results for different L_{JFET} are shown in following Table I.

Further, dynamic properties are evaluated by measuring capacitance versus drain voltage (C-V) and gate charge (Qg) characteristics. The results are shown in Fig. 3. As seen in Fig. 3(a), there is a noticeable rise in the reverse transfer capacitance (C_{rss}) as the L_{JFET} dimensions augment from 1.0μm to 2.0μm. This increase is attributed to the enlarged overlap area between the gate and drain, thereby amplifying the gate-to-drain capacitance (C_{gd}), where $C_{rss} = C_{gd}$. Additionally, Figure 3(b) highlights the output capacitance behavior (C_{oss}), which exhibits certain distinctions from C_{rss}. The C_{oss} value for L_{JFET} is at its least for 1.0μm, while L_{JFET} measuring 1.2μm and 1.4μm demonstrate nearly the same C_{oss} value at $V_{ds} = 0.1$V. L_{JFET} measuring 1.6μm, 1.8μm and 2.0μm show almost identical C_{OSS} valure. The C_{ds} value is higher for L_{JFET} measuring 1.2μm due to increased cell count with the same die size, according to the formula $C_{oss} = C_{gd} + C_{ds}$. Fig. 3(c) displays the input capacitance (C_{iss}) characteristics of DUTs. There is no obvious regular pattern of increasing L_{JFET} from 1.0μm to 2.0μm. The equation $C_{iss} = C_{gd} + C_{gs}$ shows that C_{gd} increases with L_{JFET} increment. However, C_{gs} depends on the overlap area between gate and source and the number of cells. The study measured Q_{gd} against a series of L_{JFET}, with the results presented in Fig. 3(d). A linear increase in Q_{gd} is observed with an increase in L_{JFET}, which is consistent with the previously mentioned C_{gd}.

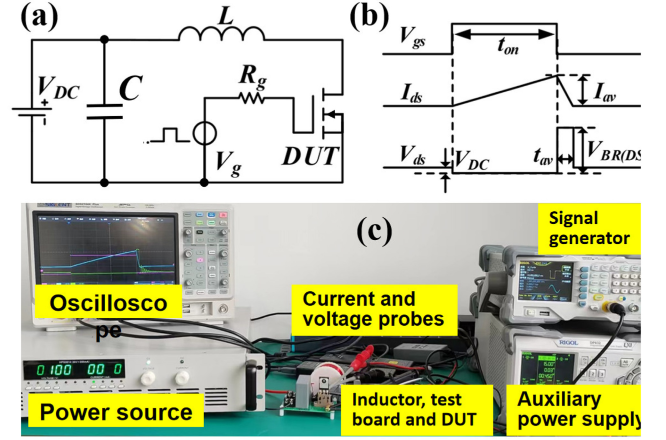

Fig. 4. (a) Simplified circuit diagram, (b) waveforms of V_{gs}, I_{ds}, and V_{ds} and (c) UIS test platform. V_{DC} = 100V, L = 2mH, V_{gs} = -5/+20V.

Table I displays the experimental results for hexagonal SiC VDMOSFETs with different L_{JFET} widths as well as for traditional linear strips with 1.4μm L_{JFET}. The JFET densities are calculated as (JFET area)/(die area). The breakdown voltage of all designs (measured at $I_{ds} = 100\mu$A) is above 1400V, which is much higher than the rating voltage of 1.2kV. And all of the threshold voltage exceed 3.2V. The measured $R_{on,sp}$ value for $L_{JFET} = 1.8\mu$m in hexagonal topology design is the smallest. For $L_{JFET} = 1.4\mu$m, the $R_{on,sp}$ in linear strip topology is 20.8m$\Omega\cdot$cm^{-2}, while it is 8.7m$\Omega\cdot$cm^{-2} in hexagonal topology. The measured HF-FOM for all hexagonal topologies are observed from $L_{JFET} = 1.0\mu$m to 2.0μm. The optimum hexagonal design with $L_{JFET} = 1.4\mu$m has better HF-FOM ($R_{on}\times C_{gd}$) by 1.96 and HF-FOM ($R_{on}\times Q_{gd}$) by 2.08 compared with the linear strip topology design.

IV. UIS EVALUATION AND RELIABILITY INVESTIGATION

The circuit schematic, principle and equipment employed for the UIS test are shown in Fig. 4. The collection of instruments comprises of an oscilloscope, high-voltage power supply, signal generator, low-voltage power supply, current probe, voltage probe, and testing board. The high-voltage power supply is responsible for generating the required bus voltage for testing purposes, which in this research is set at 100V. The signal generator supplies a drive signal to operate the DUTs in ON and OFF states, which corresponds to the inductance charging and DUT avalanche phases. The low-voltage power supply provides the voltage required for the gate driver of the DUTs. The oscilloscope displays the results of the avalanche waveform in this test. Simplified V_{gs}, I_{ds}, and V_{ds} waveforms during avalanche are seen in Fig. 4(b). When the DUT operates at the ON state, the inductor is charging and

Authorized licensed use limited to: TU Delft Library. Downloaded on July 10,2024 at 16:24:41 UTC from IEEE Xplore. Restrictions apply.

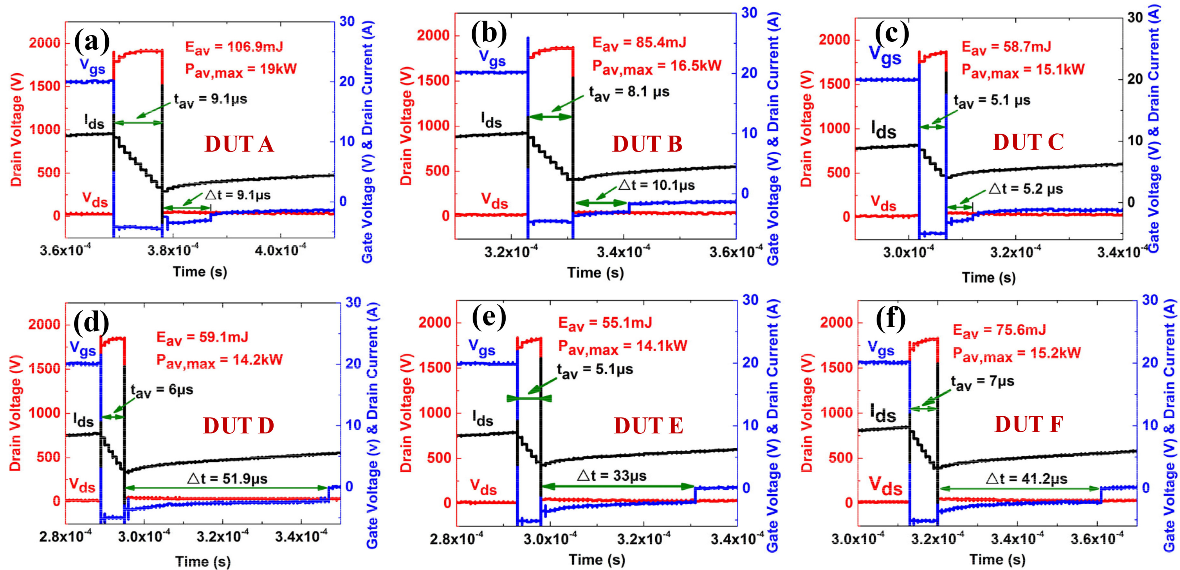

Fig. 5. Failure waveforms of various L_{JFET} during UIS experiment.

the I_{ds} rising. The I_{ds} can be obtained by flowing formula:

$$dI_{ds} = \frac{V_{DC}}{L}dt$$

When the DUT switches off and the energy stored in the inductor is released uncontrollably. A high di/dt in the inductor induces an extremely high voltage at the DUT, and the device operates on avalanche breakdown. The avalanche time (t_{av}) is calculated using the following formula:

$$t_{av} = \frac{I_{av}}{V_{BR(DSS)} - V_{DC}} \times L$$

During avalanche breakdown, the energy stored in the inductor is released into thermal dissipation in DUT until the avalanche is finished. The calculated avalanche energy (E_{av}) is as following:

$$E_{av} = \int_0^{t_{av}} V_{BR(DSS)} \cdot I_{av}(t)dt$$

where $I_{av}(t)$ is avalanche current varies with time.

V. UIS Results and Discussion

The SiC VDMOSFETs with hexagonal cell topology and different L_{JFET} widths (1.0μm, 1.2μm, 1.4μm, 1.6μm, 1.8μm, and 2.0μm) were used to investigate avalanche reliability and failure mechanism under UIS. For clarity, series of devices are designated as DUT A, DUT B, DUT C, DUT D, DUT E, and DUT F. The experimental procedure proceeds as follows: a new device is selected for the UIS test and subjected to an increasing avalanche current until failure occurs during avalanche breakdown. The electrical parameters of the final failure, including V_{gs}, I_{ds}, and V_{ds}, are extracted. This process is repeated with devices of identical specifications until consistent experimental results are achieved. The failure waveforms are shown in Fig. 5. The avalanche energy (E_{av}), maximum dissipation power during avalanche breakdown ($P_{\mathrm{av,max}}$) and avalanche duration (t_{av}) are calculated and exhibited in the picture. Burnt out time of gate voltage (Δt) is also extracted and shown in the picture. Δt describes the time from the end of the avalanche to the failure of gate. As can be seen from the picture, the voltage of all DUTs in the avalanche process is basically the same, and they are all around 1750V. And as the avalanche breakdown continues, the voltage gradually rises. This is because a lot of heat is generated in DUTs during avalanche process, causing the avalanche breakdown voltage of silicon carbide to rise. Notably, DUT A had the largest E_{av} at 106.9mJ. The E_{av} of DUT B, C, D, E and F are 85.4mJ, 58.7mJ, 59.1mJ, 55.1mJ and 75.6mJ, respectively. The avalanche energy is converted into loss during avalanche breakdown. The larger the $E_{\mathrm{av},}$ the more severe the heat loss experienced by the device during the avalanche process. At the same time, the maximum power loss of the device in the process of avalanche breakdown is calculated according to $P_{\mathrm{av,max}}$ = U × I formula. U is the V_{ds} during avalanche breakdown, and I is the I_{ds}. E_{av} is used to evaluate the heat generated, while $P_{\mathrm{av,max}}$ is used to evaluate the maximum dissipation power during avalanche. The larger $P_{\mathrm{av,max}}$, the faster heating rate, which also means the greater thermal shock. DUT A has a $P_{\mathrm{av,max}}$ of 19kW, indicating that the device experiences the greatest instantaneous thermal shock inside the material. The $P_{\mathrm{av,max}}$ of DUT B, C, D, E and F are 16.5kW, 15.1kW, 14.2kW, 14.1kW and 15.2kW respectively. As can be seen from the picture, the avalanche energy is positively correlated with the avalanche breakdown time. The greater avalanche energy, the longer avalanche lasts. DUT A has a t_{av} of 9.1μs and DUT B has a t_{av} of 8.1μs.

After dropping the t_{av}, the V_{ds} drops from the avalanche breakdown voltage to zero, but the I_{ds} is out of control. At this moment, the V_{gs} begins to gradually rise from $-$5V. And V_{gs} increased with the increase of time. The possible reason is that due to the avalanche breakdown and I_{ds} out of control, the temperature of the DUTs increases sharply, and the schottky

Authorized licensed use limited to: TU Delft Library. Downloaded on July 10,2024 at 16:24:41 UTC from IEEE Xplore. Restrictions apply.

TABLE II
SUMMARY OF UIS EXPERIMENT RESULTS

Design	E_{av} (mJ)	t_{av} (μs)	$P_{av,max}$ (kW)	Δt (μs)
DUT A	106.9	9.1	19	9.1
DUT B	85.4	8.1	16.5	10.1
DUT C	58.7	5.1	15.1	5.2
DUT D	59.1	6	14.2	51.9
DUT E	55.1	5.1	14.1	33
DUT F	75.6	7	15.2	41.2

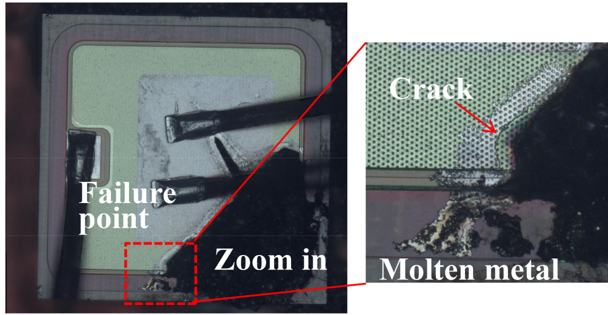

Fig. 6. Optical microscope images and zoom in for failed device.

current increases under gate oxide while the driver power remains unchanged, resulting V_{gs} increase. After Δt, the V_{gs} suddenly rises sharply, meaning the device damage. It is worth noting that the Δt varies with different designs and it does not seem to be related to E_{av}. DUT A, B, and C have similar Δt values of 9.1μs, 10.1μs, and 5.2μs, respectively. However, in DUT D, E, and F, Δt are 51.9μs, 33μs, and 41.2μs, respectively, which is almost 4 times that of DUT A and more than 6 times that of DUT C. It is well known that devices are mainly caused by thermal runaway in UIS tests. However, such a large Δt means that there may be some different failure mechanisms between DUT A, B, C and DUT D, E, F. For clarity, UIS experiment results are summarized in Table II.

Further, all the DUTs after avalanche failure are decapsulated. We compared all the failure devices, and found that the failure location is random. One of the optical microscope image is shown in Fig. 6. A failure position point located at the lower right corner of the chip. The black material is carbonized after the ablation of the molding compound and can not be cleaned by chemical solution, meaning that the device experienced extremely high temperature during avalanche process. The failure location point is scaled up, as seen in the picture, the metal melts and flows to the terminal insulation area from active region. In addition, there is a crack along the residual edge of the molding compound that spans many cells in length. The random failure position can be explained from that some defects in the chip are randomly distributed due to manufacturing process fluctuations, resulting low blocking voltage capacity of some cells. And the avalanche occurs first in those weak cells under the UIS test. During avalanche breakdown, the energy stored in the inductor is released instantaneously to heat in those cells, resulting in extremely high temperature thermal shock in the device and internal

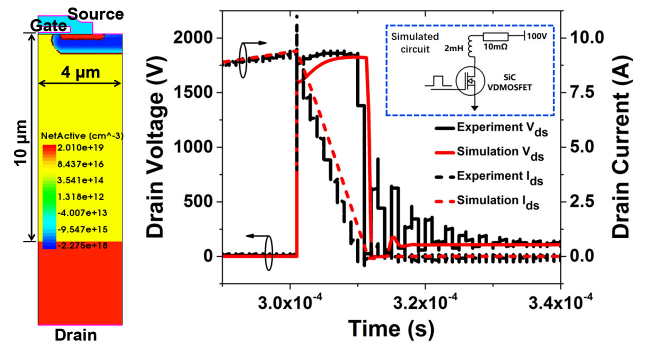

Fig. 7. I_{ds} and V_{ds} of half-cell simulation results for DUT C under the UIS test before avalanche failure.

cracking between the materials. The results are consistent with those reported in previous studies [16].

Further, the half-cell structure SiC VDMOSFETs was constructed according to the experimental structure and parameters by TCAD. Mixe-mode module was applied in TCAD simulation, and the simulated circuit was shown in Fig. 7. Besides, the self-heating model is considered in the simulation. Considering that there is resistance in the actual circuit, 10mΩ resistance is introduced in the simulation circuit diagram. The inductance L (2mH) in the simulation is the same as that in the actual test. The figure shows the match between the experimental test waveform and the simulation waveform of DUT C before the failure. The zigzag in the experimental waveform is due to the low bandwidth of the oscilloscope. It can be seen from the figure that there is a good agreement between the simulated waveform and the actual waveform, which means that the simulation can qualitatively determine the changes between the internal physical quantities of the device in the UIS working process.

Fig. 8 shows the failure mechanism of DUT during avalanche breakdown by using TCAD simulation. Fig. 8 (a) shows the simulated waveform of DUT C avalanche failure. t1 and t2 in Fig. 8(a) represent two moments are used to explore how the physical parameters change in the device. Fig. 8(b) shows the cell structure and circuit schematic of SiC VDMOSFET and current path at t1 and t2. As shown in Fig. 8(c), during avalanche breakdown (t1), the avalanche current flows from the drain through the P-Based region to the source to release avalanche energy. However, between t1 and t2, the channel is opened and the avalanche current exists at both the P-Based and the channel region. The reason is that a lot of heat is generated during avalanche breakdown, leading to R_B rise. When the voltage between R_B exceeds 2.7V (PN junction drop voltage in SiC), the parasitic BJT is ON, resulting in I_{ds} uncontrollable. t2 point indicates that the I_{ds} is uncontrollable. This phenomenon is confirmed by experimental waveform in Fig. 5.

As I_{ds} is out of control, the internal temperature of the device is further increased sharply. Fig. 8 (d) shows the internal temperature distribution at t1, t1∼t2, and t2. It can be seen from the picture that the highest temperature is mainly concentrated in the JFET region. And with the increase of

Authorized licensed use limited to: TU Delft Library. Downloaded on July 10,2024 at 16:24:41 UTC from IEEE Xplore. Restrictions apply.

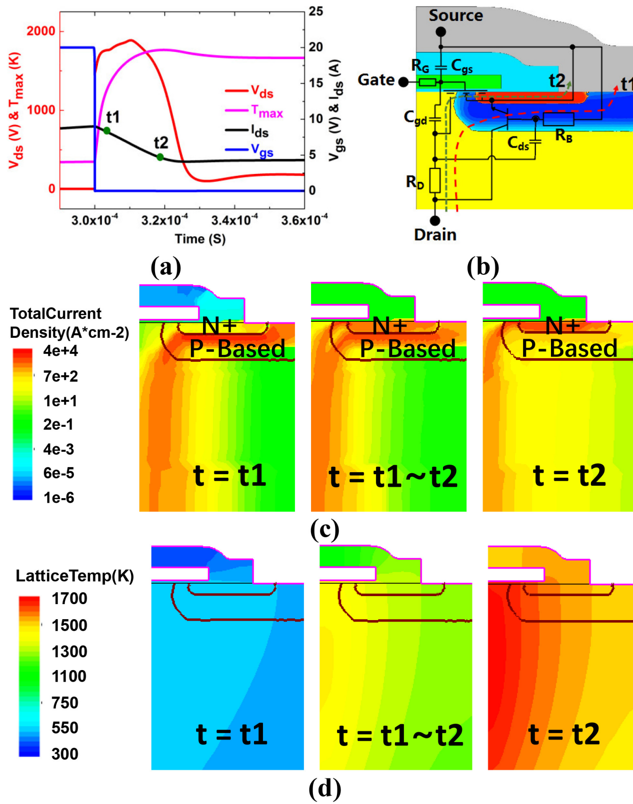

Fig. 8. (a) Simulated waveform for DUT C during avalanche failure. (b) Simulated results circuit schematics and avalanche current paths. (c) Current density within device, and (d) lattice temperature distribution at time point t1, t1∼t2, and t2.

time from t1 to t2, the lattice temperature rises sharply. At t2, the highest temperature reached 1700K, exceeding the melting point of aluminum. The optical microscopic image in Fig. 6 confirms this conclusion. A conjure is proposed that cracks occur inside the material due to sharply internal thermal stress, resulting in device damage. As time increases, the maximum temperature expands from the JFET region to the source contact. The larger L_{JFET}, the longer it takes for the temperature to spread. Therefore, the Δt of DUT F is much longer than that of DUT A in Fig. 5.

VI. Conclusion

In this paper, the hexagonal cell topology of planar SiC VDMOSFETs with varied L_{JFET} are designed and manufactured. The static properties, dynamic characteristics, and UIS test are investigated. $L_{JFET} = 1.4\mu$m has the best HF-FOM by comparing the dynamic and static parameters of each design. The reliability and failure mechanism of different designs under UIS test were investigated by experiment and TCAD simulation. During avalanche process, the device generates a lot of heat instantaneously, resulting in parasitic BJT conduction, current out of control and failure. The instantaneous extreme high temperature causes internal cracking of the material and metal melting, resulting in device damage. Besides, The heat is mainly concentrated in the JFET region during avalanche breakdown. V_{gs} mutates after the current is out of control since that molten metal contacts the gate through a crack, resulting in gate-source short circuit.

References

[1] E. Manikandan and L. Agarwal, "A comprehensive review of recent progress, prospect and challenges of silicon carbide and its applications," *Silicon*, vol. 14, no. 18, pp. 12887–12900, 2022, doi: 10.1007/s12633-022-01998-9.

[2] X. She, A. Q. Huang, O. Lucia, and B. Ozpineci, "Review of silicon carbide power devices and their applications," *IEEE Trans. Ind. Electron.*, vol. 64, no. 10, pp. 8193–8205, Oct. 2017, doi: 10.1109/tie.2017.2652401.

[3] K. Puschkarsky, T. Grasser, T. Aichinger, W. Gustin, and H. Reisinger, "Review on SiC MOSFETs high-voltage device reliability focusing on threshold voltage instability," *IEEE Trans. Electron Devices*, vol. 66, no. 11, pp. 4604–4616, Nov. 2019, doi: 10.1109/ted.2019.2938262.

[4] L. Di Benedetto, G. D. Licciardo, T. Erlbacher, A. J. Bauer, R. Liguori, and A. Rubino, "A model of electric field distribution in gate oxide and JFET-region of 4H-SiC DMOSFETs," *IEEE Trans. Electron Devices*, vol. 63, no. 9, pp. 3795–3799, Sep. 2016, doi: 10.1109/ted.2016.2584218.

[5] D. Kim, N. Yun, A. J. Morgan, and W. Sung, "The effect of deep JFET and P-well implant of 1.2kV 4H-SiC MOSFETs," *IEEE J. Electron Devices Soc.*, vol. 10, pp. 989–995, Nov. 2022, doi: 10.1109/jeds.2022.3218689.

[6] A. Agarwal, K. Han, and B. J. Baliga, "Comparison of 2.3-kV 4H-SiC Accumulation-channel planar power MOSFETs fabricated with linear, square, hexagonal, and octagonal cell topologies," *IEEE Trans. Electron Devices*, vol. 67, no. 9, pp. 3673–3678, Sep. 2020, doi: 10.1109/ted.2020.3005632.

[7] K. Han and B. J. Baliga, "Comparison of four cell topologies for 1.2-kV accumulation- and inversion-channel 4H-SiC MOSFETs: Analysis and experimental results," *IEEE Trans. Electron Devices*, vol. 66, no. 5, pp. 2321–2326, May 2019, doi: 10.1109/ted.2019.2905736.

[8] D. Kim et al., "A static, switching, short-circuit characteristics of 1.2 kV 4H-SiC MOSFETs: Comparison between linear and (bridged) hexagonal topology," presented at the 2021 IEEE 8th Workshop Wide Bandgap Power Devices Appl. (WiPDA), 2021.

[9] K. Yao, H. Yano, H. Tadano, and N. Iwamuro, "Investigations of SiC MOSFET short-circuit failure mechanisms using electrical, thermal, and mechanical stress analyses," *IEEE Trans. Electron Devices*, vol. 67, no. 10, pp. 4328–4334, Oct. 2020, doi: 10.1109/ted.2020.3013192.

[10] J. A. Schrock et al., "Failure analysis of 1200-V/150-A SiC MOSFET under repetitive pulsed overcurrent conditions," *IEEE Trans. Power Electron.*, vol. 31, no. 3, pp. 1816–1821, Mar. 2016, doi: 10.1109/tpel.2015.2464780.

[11] M. D. Kelley, B. N. Pushpakaran, and S. B. Bayne, "Single-Pulse avalanche mode robustness of commercial 1200 V/80 mΩ SiC MOSFETs," *IEEE Trans. Power Electron.*, vol. 32, no. 8, pp. 6405–6415, Aug. 2017, doi: 10.1109/tpel.2016.2621099.

[12] T.-T. Nguyen, A. Ahmed, T. V. Thang, and J.-H. Park, "Gate oxide reliability issues of SiC MOSFETs under short-circuit operation," *IEEE Trans. Power Electron.*, vol. 30, no. 5, pp. 2445–2455, May 2015, doi: 10.1109/tpel.2014.2353417.

[13] J. Naghibi, S. Mohsenzade, K. Mehran, and M. P. Foster, "Gate oxide degradation condition monitoring technique for high-frequency applications of silicon carbide power MOSFETs," *IEEE Trans. Power Electron.*, vol. 38, no. 1, pp. 1079–1091, Jan. 2023, doi: 10.1109/tpel.2022.3198291.

[14] C. Lin, N. Ren, H. Xu, and K. Sheng, "Performance and short-circuit reliability of SiC MOSFETs with enhanced JFET doping design," *IEEE Trans. Electron Devices*, vol. 70, no. 5, pp. 2395–2402, May 2023, doi: 10.1109/ted.2023.3259925.

[15] Z. Zhu, N. Ren, H. Xu, L. Liu, and K. Sheng, "Characterization and analysis on performance and avalanche reliability of SiC MOSFETs with varied JFET region width," *IEEE Trans. Electron Devices*, vol. 68, no. 8, pp. 3982–3990, Aug. 2021, doi: 10.1109/ted.2021.3091043.

[16] Z. Bai et al., "Investigation on single pulse avalanche failure of 1200-V SiC MOSFETs via optimized thermoelectric simulation," *IEEE Trans. Electron Devices*, vol. 68, no. 3, pp. 1168–1175, Mar. 2021, doi: 10.1109/ted.2020.3048921.

Authorized licensed use limited to: TU Delft Library. Downloaded on July 10,2024 at 16:24:41 UTC from IEEE Xplore. Restrictions apply.